JACS
JOURNAL OF THE AMERICAN CHEMICAL SOCIETY
Article
pubs.acs.org/JACS

Hybrid Cellular Nanosheets for High-Performance Lithium-Ion Battery Anodes

Seung-Ho Yu,[†,‡,⊥] Dong Jun Lee,[†,‡,⊥] Mihyun Park,[†,‡] Soon Gu Kwon,[†,‡] Hyeon Seok Lee,[†,‡] Aihua Jin,[†,‡] Kug-Seung Lee,[§] Ji Eun Lee,[†,‡,#] Myoung Hwan Oh,[†,‡] Kisuk Kang,[†,∥] Yung-Eun Sung,[*,†,‡] and Taeghwan Hyeon[*,†,‡]

[†]Center for Nanoparticle Research, Institute for Basic Science (IBS), Seoul 151-742, Republic of Korea

[‡]School of Chemical and Biological Engineering, Institute of Chemical Processes and [∥]Department of Materials Science and Engineering, Seoul National University, Seoul 151-742, Republic of Korea

[§]Beamline Department, Pohang Accelerator Laboratory (PAL), Pohang 790-784, Republic of Korea

[#]Creative and Fundamental Research Division, Korea Electrotechnology Research Institute (KERI), Changwon 641-120, Republic of Korea

Supporting Information

ABSTRACT: We report a simple synthetic method of carbon-based hybrid cellular nanosheets that exhibit outstanding electrochemical performance for many key aspects of lithium-ion battery electrodes. The nanosheets consist of close-packed cubic cavity cells partitioned by carbon walls, resembling plant leaf tissue. We loaded carbon cellular nanosheets with SnO_2 nanoparticles by vapor deposition method and tested the performance of the resulting SnO_2–carbon nanosheets as anode materials. The specific capacity is 914 mAh g^{-1} on average with a retention of 97.0% during 300 cycles, and the reversible capacity is decreased by only 20% as the current density is increased from 200 to 3000 mA g^{-1}. In order to explain the excellent electrochemical performance, the hybrid cellular nanosheets were analyzed with cyclic voltammetry, in situ X-ray absorption spectroscopy, and transmission electron microscopy. We found that the high packing density, large interior surface area, and rigid carbon wall network are responsible for the high specific capacity, lithiation/delithiation reversibility, and cycling stability. Furthermore, the nanosheet structure leads to the high rate capability due to fast Li-ion diffusion in the thickness direction.

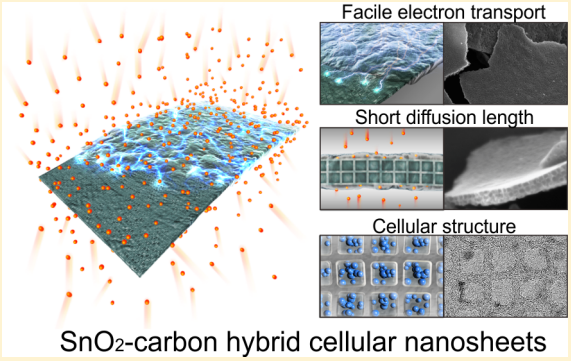

INTRODUCTION

The development of next-generation energy-storage devices is of primary importance to meet the challenges in the electronics and automobile industries in the near future.[1−6] In particular, there has been increasing interest in the development of new multicomponent nanomaterials that can overcome a number of intrinsic limitations of single-component electrode materials for lithium-ion batteries (LIBs).[7−11] The considerable volume changes of the active materials from lithiation and delithiation lead to the mechanical deformation, causing the high internal resistance and low cycle stability. This is especially pronounced for the high-capacity anode materials such as Si,[12−16] Ge,[17−19] Sn,[20] SnO_2,[21−24] and Fe_2O_3[25−28] because they have a very large volume change during cycling. Also, the side reactions at the interface between the electrolyte and the active material can decrease in the Coulombic efficiency and cause safety problems.[29−31] Since the early 2000s, multicomponent nanostructures that consist of hollow carbon shell encapsulating active materials have attracted strong interest because they can provide very effective solutions to these limitations of anode materials.[32−42] In this structure, the carbon shell confines the active material within a closed volume so that the loss of capacity due to pulverization and agglomeration can be minimized and good electric contact with the active material can be ensured during cycling. Furthermore, the assembled structure of carbon shells can reduce the contact area between the electrolyte and the active materials inside of the shell, reducing the formation of the solid–electrolyte interphase (SEI). Also, the extended carbon network of the assembled structure can facilitate the electron transport.[43,44] Thus far, various carbon-based multicomponent hybrid nanostructures for LIB anodes have been reported to exhibit high electrochemical performance in either long stability, high capacity, or high rate capability.[45−50] On the basis of these previous reports, an ideal hybrid nanostructure that combines key aspects of the electrode materials including cycling stability, specific capacity, and rate performance is highly anticipated.

Herein, we report a new synthetic method of carbon-based hybrid nanosheets that exhibit outstanding performance in

Received: April 8, 2015
Published: September 1, 2015

DOI: 10.1021/jacs.5b03673
J. Am. Chem. Soc. 2015, 137, 11954−11961

many key aspects of the LIB anode. While the synthetic procedure is simple and straightforward without any separate assembly process, as-prepared nanosheets have close-packed uniform cubic empty "cells" of ~12 nm side length that are enclosed by 3.5 nm thick carbon walls. The inorganic anode materials are incorporated into the empty cells by simple vapor deposition. Our preparation method is easier and simpler than that of the previously reported hybrid nanomaterials.[45−50] The cubic cells enclosed by the carbon walls provide enough space for the volume change of the inorganic active material inside and retain the mechanical integrity during lithiation and delithiation. Also, the cubic shape ensures the maximum packing density and the larger contact area with the active material compared to the spherical shape with the same volume. The nanosheet structure provides a short diffusion length of Li ions in the thickness direction and facile electron transport through its carbon network which is as large as hundreds of square micrometers. As a model system, we investigated the electrochemical properties of hybrid cellular nanosheets loaded with tin dioxide nanoparticles (SnO_2 NPs). The cell tests showed a high specific capacity of 913.9 mAh g^{-1} on average with excellent cycle retention of 97.0% during 300 cycles when applied to LIB anodes. Also, when the cycling current density was increased from 200 to 3000 mA g^{-1}, the reversible capacity was decreased by only 20% from 941.3 to 745.5 mAh g^{-1}. As a result, our hybrid cellular nanosheets showed outstanding performance in the key aspects of the LIB anode by the well-optimized carbon-based hybrid structure.

RESULTS AND DISCUSSION

Synthesis and Characterization of Hybrid Cellular Nanosheets. The synthesis of carbon cellular nanosheets is accomplished by a modification of the previously reported method from our group.[51,52] In the first step, carbon nanosheets embedded with manganese ferrite ($MnFe_2O_4$) nanocubes are synthesized by heating a mixture of manganese− and iron−oleate precursors and sodium sulfate (Na_2SO_4) powder at 500 °C for 5 h under inert atmosphere. During the heating process, both the formation of $MnFe_2O_4$ nanocubes and their self-assembly take place at the surface of the sodium salt particles. At the same time, oleate ligands that cover the surface of the nanocubes are carbonized into the nanosheets. After the heating procedure, Na_2SO_4 powder and the ferrite nanocubes are removed by washing with water and acid etching, respectively, leaving the carbon cellular nanosheets (see Experimental Section for experimental details). Compared to ferrite−carbon hybrid nanosheets synthesized using only iron−oleate complex, smaller sized nanocubes can be obtained using a mixture of manganese− and iron−oleate complexes,[52] which is advantageous for lithium-ion battery application.

The porous structure of the carbon cellular nanosheets consists of uniform cubic empty "cells" of ~12 nm side length that are enclosed by 3.5 nm thick carbon walls (Figure 1a and 1b). The cells form ordered arrays over the whole area of the nanosheets that is as large as hundreds of square micrometers. The cross-section of a nanosheet in the scanning electron microscopy (SEM) image (Figure 1c) shows that the thickness is ~100 nm, which corresponds to <10 layers of the cells (see Figures S1 and S2 in the Supporting Information for additional electron microscopy images and small-angle X-ray scattering data of the carbon cellular nanosheets). Actually, this structure resembles the plant leaf tissue that is composed of the two-dimensional array of cells partitioned by cell walls (Figure 1d−f).

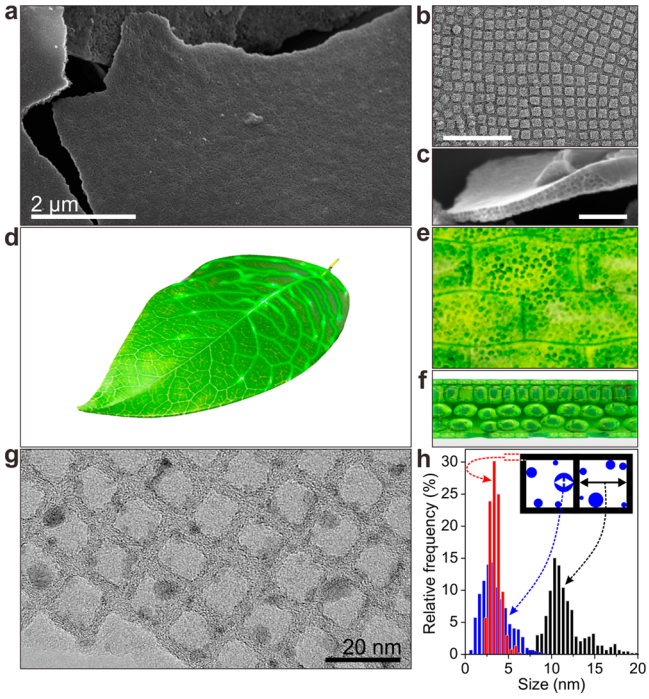

Figure 1. Carbon and SnO_2−carbon cellular nanosheets. (a) SEM image, (b) TEM image, and (c) cross-sectional SEM image of carbon cellular nanosheets. Scale bars in b and c are 100 and 200 nm, respectively. Schematic illustration of (d) a plant leaf, (e) its top, and (f) cross-sectional structures resembling the carbon cellular nanosheets. (g) TEM image of a SnO_2−carbon hybrid cellular nanosheet showing SnO_2 NPs in the cells. (h) Statistical analysis of the size of SnO_2 NPs (blue), side length of the cells (black), and thickness of the carbon walls (red).

Hybrid cellular nanosheets were prepared by introducing SnO_2 as high-capacity anode material inside the carbon cells via vapor deposition using tetraphenyltin [$Sn(C_6H_5)_4$] as a precursor. This method is inspired from the well-known "ship-in-a-bottle" approach which is used for incorporation of various materials into the pores/cages of zeolites[53] or mesoporous materials.[54] The carbon cellular nanosheets are mixed with tetraphenyltin and heated at 350 °C for 3 h under vacuum. In this condition, vaporized tin precursor infiltrated inside of the cells and subsequently turns into SnO_2 NPs via thermal decomposition. The remaining unreacted precursor is evaporated away, leaving no residue on the exterior surface of the nanosheets. Figure 1g shows the transmission electron microscopy (TEM) image of SnO_2 NPs formed in the cells (see Figure S3 in the Supporting Information for the low-magnification TEM image of a SnO_2−carbon hybrid cellular nanosheet). The statistics of the size of SnO_2 NPs, the side length of the empty cells, and the wall thickness are shown in Figure 1h. The size of the NPs is far smaller than the cavity volume of the cells. Since the lithiation of SnO_2 NPs increases the volume by 300%, such a large difference in the cavity volume and the NPs is beneficial for better mechanical stability and reversible capacity of the electrode, as we will discuss below.

Detailed structure analysis of the carbon cellular nanosheets before and after incorporating SnO_2 by the "ship-in-a-bottle" method was performed by various techniques, and the results

DOI: 10.1021/jacs.5b03673
J. Am. Chem. Soc. 2015, 137, 11954−11961

are shown in Figure 2. The pore size and volume of the cellular nanosheets are analyzed by N_2 adsorption and desorption

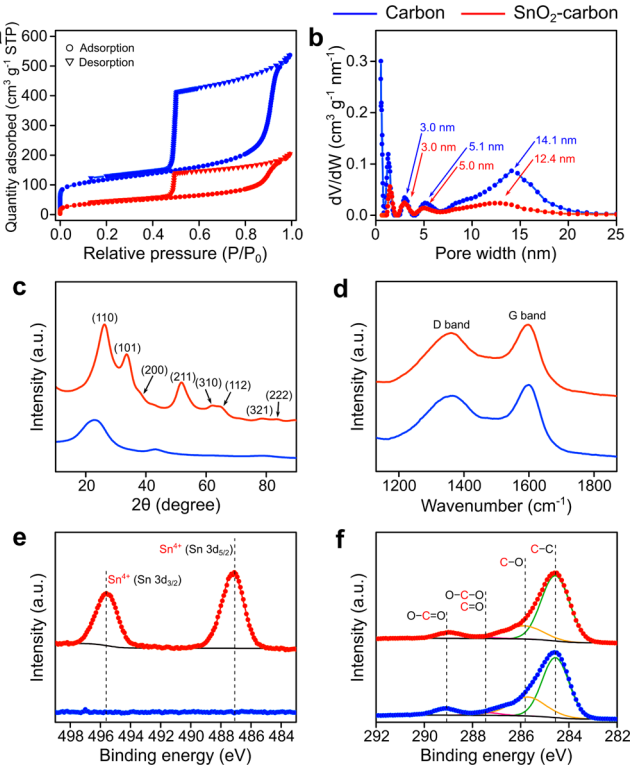

Figure 2. Structure analysis of carbon and SnO_2–carbon cellular nanosheets. For all panels, blue indicates carbon cellular nanosheets and red represents SnO_2–carbon cellular nanosheets. N_2 adsorption–desorption isotherms (a) and pore size distributions from the isotherm curves (b). (c) XRD plots. Diffraction peaks from SnO_2–carbon nanosheets are indexed to tetragonal SnO_2. (d) Raman spectra. Bands at around 1600 and 1360 cm^{-1} are assigned to G and D bands of graphite structure. (e, f) XPS spectra from Sn 3d (e) and C 1s (f). Peaks are assigned by curve fittings indicated in different colors.

isotherm measurements (Figures 2a and 2b). Before incorporation, pores with sizes of 3.0, 5.1, and 14.1 nm were identified from the carbon cellular nanosheets. The size of the largest pores (14.1 nm) matches the cubic cell size measured by TEM (~12 nm). After loading the NPs, the size of the largest pores was decreased to 12.4 nm and the pore volume was changed from 0.71 to 0.28 $cm^3\ g^{-1}$. The reduction in both the pore size and the volume is consistent with the observation from TEM that the cubic empty cells were occupied by the NPs.[55,56] X-ray diffraction (XRD) data from carbon and SnO_2–carbon nanosheets are shown in Figure 2c. The two broad peaks from the carbon nanosheets at $2\theta = 23°$ and 42° are assigned to the (002) and (101) planes of carbon.[57] On the other hand, the pattern of SnO_2–carbon nanosheets is clearly indexed to tetragonal SnO_2 (JCPDS card no. 41-1445). Raman spectroscopy data show that the peak intensity ratio of D and G bands from carbon (I_D/I_G) is almost identical in the spectra from carbon and SnO_2–carbon nanosheets (Figure 2d), showing that the impregnation process does not affect the carbon structure of the nanosheets. After impregnation, a signal from Sn^{4+} is observed in the Sn 3d region by X-ray photoelectron spectroscopy (XPS), confirming the presence of SnO_2 phase in the nanosheets (Figure 2e).[58] C 1s XPS data reveal that there are oxygen functional groups such as C–O and O–C=O in the carbon nanosheets, probably due to the acid etching treatment (Figure 2f). These oxygen functional groups can help the formation of SnO_2 NPs at the interior wall of the carbon cells (see Figure S4a in the Supporting Information for the corresponding wide-scan XPS of Figure 2e and 2f).[59,60] According to thermogravimetric analysis (TGA), the carbon nanosheets contain no inorganic impurity while the content of SnO_2 in SnO_2–carbon nanosheets is 38.0 wt % (Figure S4b in the Supporting Information). The content of SnO_2 can be controlled by varying the ratio of carbon nanosheets to precursor and/or by repeating the deposition process (Figure S5).

Electrochemical Performance of Hybrid Cellular Nanosheets. The electrochemical performance of SnO_2–carbon hybrid cellular nanosheets was investigated by a series of experiments in comparison with the carbon cellular nanosheets and SnO_2 nanosheets. SnO_2 nanosheets are prepared by heating SnO_2–carbon hybrid cellular nanosheets at 500 °C in air, leading to the formation of the nanosheets of sintered SnO_2 NPs (see Figure S6 in the Supporting Information for TEM images and XRD data of SnO_2 nanosheets). The electrochemical cycling stability of SnO_2–carbon hybrid, carbon, and SnO_2 nanosheets was evaluated by galvanostatic charging–discharging in a potential range of 0.01–3.0 V (vs Li^+/Li) at a constant current density of 200 mA g^{-1} (Figure 3a). After 300 cycles, the reversible capacity of SnO_2–carbon hybrid nanosheets is changed from 941.3 (1st cycle) to 913.3 mAh g^{-1} (300th cycle), showing outstanding cycle retention of 97.0%. The average capacity value of the hybrid nanosheets is higher than those from the previously reported SnO_2–carbon nanostructures.[61−64] Carbon cellular nanosheets also exhibit relatively high cycling stability with a retention of 86.6% during 300 cycles, and the average capacity was 463.0 mAh g^{-1}. On the other hand, the capacity of SnO_2 nanosheets rapidly decreases during the first 50 cycles from 882.2 (1st cycle) to 141.1 mAh g^{-1} (50th cycle). The overall features of initial charge–discharge voltage profiles of SnO_2–carbon hybrid nanosheets are similar to those of other SnO_2–carbon composite materials in the previous reports (Figure S7).[49,61] The initial discharge capacity and Coulombic efficiency are 1910.7 mAh g^{-1} and 49.3%, respectively. As shown in Figure 3b, the voltage profiles of SnO_2–carbon hybrid nanosheets are so stable that the profile plots from the 100th to the 200th cycle are almost exactly overlapped on top of each other. Even at very high current densities of 1000 and 3000 mA g^{-1}, the hybrid cellular nanosheets exhibit high reversible capacities of 815.1 and 745.5 mAh g^{-1}, respectively (Figure 3c). It can therefore be concluded that the electrochemical properties of hybrid cellular nanosheets are comprehensively outstanding when compared with the other SnO_2-based anode materials.

The lithiation and delithiation of SnO_2 NPs in the hybrid cellular nanosheets were investigated by cyclic voltammetry and in situ X-ray absorption near-edge structure (XANES) spectroscopy. It is known that there are two reactions between lithium and SnO_2 taking place during charging and discharging processes[65]

$$SnO_2 + 4Li^+ + 4e^- \rightarrow Sn + 2Li_2O \quad (1)$$

$$Sn + xLi^+ + xe^- \rightleftarrows Li_xSn\ (0 \le x \le 4.4) \quad (2)$$

Usually reaction 1 is considered to be irreversible, while reaction 2 is responsible for the theoretical reversible capacity of 782 mAh g^{-1}. However, recently it was reported that

DOI: 10.1021/jacs.5b03673
J. Am. Chem. Soc. 2015, 137, 11954–11961

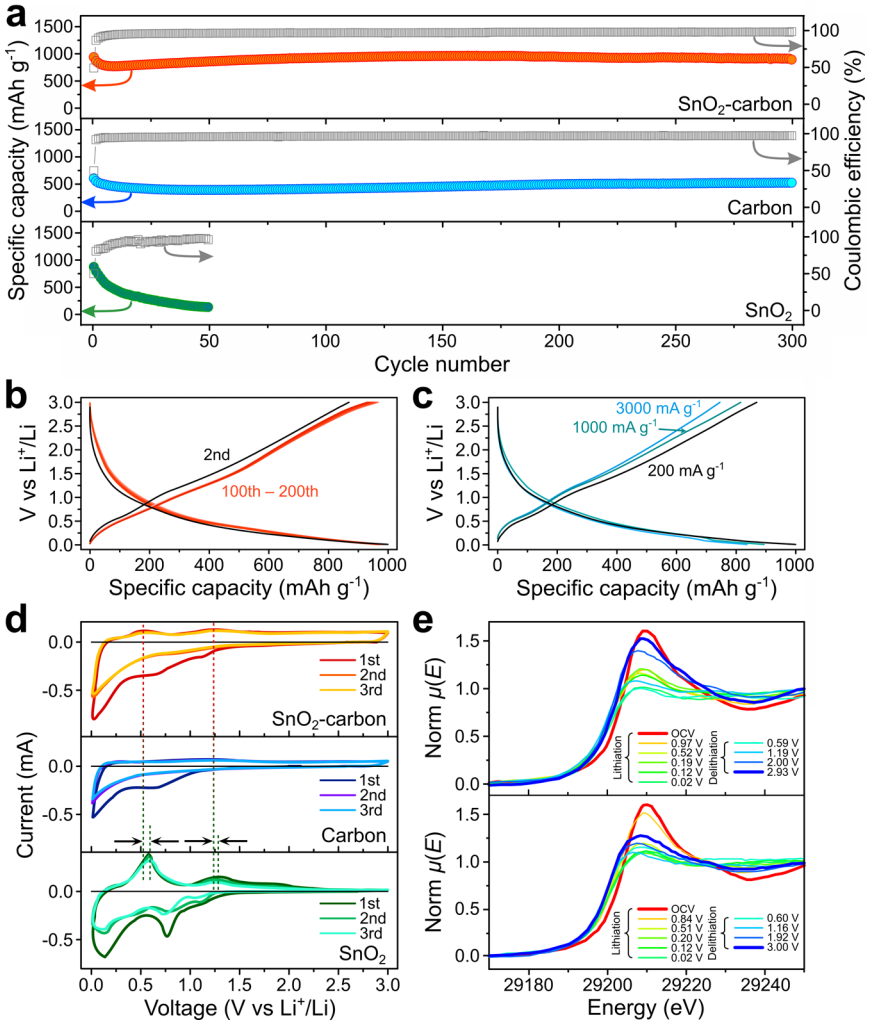

Figure 3. Electrochemical characterization of SnO_2−carbon, carbon, and SnO_2 nanosheets for lithium-ion battery anodes. (a) Cycling performance of the three kinds of nanosheets. (b) Voltage profiles of SnO_2−carbon nanosheets corresponding to the SnO_2−carbon data in a. (a, b) Current density was 200 mA g^{-1}. (c) Voltage profiles of SnO_2−carbon nanosheets at three current densities in the second cycle. Black profile curves in b and c are identical. (d) Cyclic voltammogramms of the nanosheets. Scan rate was 0.1 mV s^{-1}. The shift in the current peak positions is indicated with arrows. (e) In situ Sn K edge XANES data of SnO_2−carbon and SnO_2 nanosheets measured during the first cycle at a current density of 200 mA g^{-1} and the voltage range of 0.01−3.0 V (vs Li^+/Li). OCV indicates the XANES patterns measured just before starting the cycle.

reaction 1 is partially reversible and contributing to the capacity of SnO_2.[66,67] Figure 3d shows three initial consecutive cyclic voltammograms of the three nanosheets. The cyclic voltammograms of SnO_2−carbon hybrid cellular nanosheets have the features from both carbon and SnO_2 nanosheets. However, the anodic peaks at 0.53 and 1.23 V from SnO_2−carbon nanosheets are shifted to lower potentials compared to those from SnO_2 nanosheets that are observed at 0.58 and 1.25 V, respectively. The lower polarization suggests that the reaction of SnO_2 in the hybrid nanosheets is different from that of pure SnO_2. In order to investigate the electrochemical reaction process of SnO_2 in detail, the temporal change in the oxidation state of Sn during cycling was investigated by in situ XANES measurements. As shown in Figure 3e, the white line intensities of the signals from SnO_2−carbon hybrid nanosheets measured at the start and the end of the cycling are quite similar. On the other hand, the white line intensity from SnO_2 nanosheets becomes far weaker after one cycle. Such difference in the white line intensity is attributed to the different oxidation state of Sn in the nanosheets. According to the linear combination fit analysis using Sn metal, SnO, and SnO_2 as the standards, both the hybrid nanosheets and SnO_2 nanosheets contain only SnO_2 before cycling (see Figure S8 in the Supporting Information for the standard XANES data of Sn metal, SnO, and SnO_2). However, after one cycle, the ratio of Sn:SnO:SnO_2 was changed to 0:45:55 for the hybrid nanosheets and 26:51:23 for SnO_2 nanosheets, demonstrating that tin oxide in the hybrid nanosheets can have better reversibility of the electrochemical reactions. In particular, it seems that a considerable amount of metallic Sn is oxidized to SnO_2 via reaction 1 during delithiation of the hybrid nanosheets.

Structural Change of Hybrid Cellular Nanosheets by Lithiation and Delithiation. Changes in the structure of SnO_2−carbon hybrid cellular nanosheets induced by cycling were studied by extensive TEM analysis. As mentioned above, insertion of lithium into SnO_2 leads to the formation of Li_xSn ($x \leq 4.4$) embedded in Li_2O matrix which is accompanied by a large volume expansion of ~300%. TEM images in Figure 4a−c show how the size and morphology of SnO_2 NPs in the nanosheets change during lithiation and delithiation. When fully lithiated (0.01 V vs Li^+/Li), SnO_2 NPs are expanded, almost completely filling the volume of the cell (Figure 4b).

DOI: 10.1021/jacs.5b03673
J. Am. Chem. Soc. 2015, 137, 11954−11961

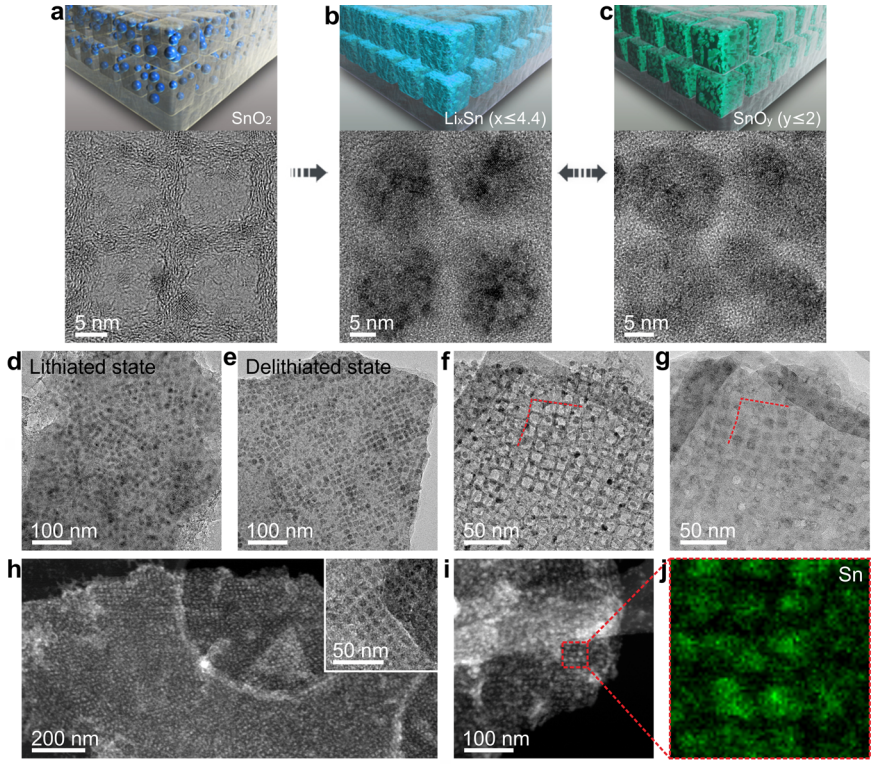

Figure 4. TEM analysis on the structural change of hybrid cellular nanosheets. Schematics of the morphology of SnO_2 NPs and SnO_2-based active material structure in the carbon cells (top), and TEM images of hybrid cellular nanosheets (bottom) before cycling (a), after lithiation (b), and after delithiation (c). TEM images of hybrid cellular nanosheets after lithiation (d) and delithiation (e). TEM images of hybrid cellular nanosheets before (f) and after (g) one cycle of lithiation and delithiation from the same location. Red-dotted line indicates the same position on the nanosheet. (h) Dark-field scanning TEM image of hybrid cellular nanosheets after 20 cycles. (Inset) TEM image after 20 cycles. Dark-field scanning TEM image (i) and EDX mapping of Sn L_{III} edge (j) after 20 cycles. EDX mapping was performed in the red-dotted square in i.

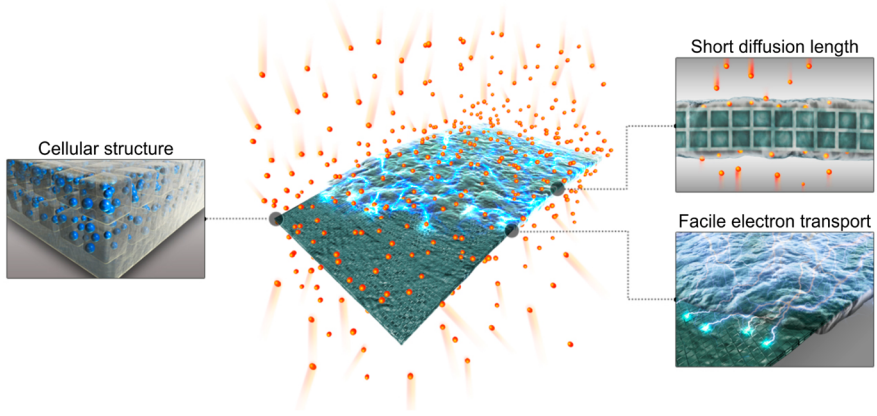

Figure 5. Illustration of a SnO_2–carbon hybrid cellular nanosheet and its features that contribute to the electrochemical performance.

Interestingly, delithiation does not restore the NPs with the initial size and shape. Instead, SnO_2-based active material is coated inside the wall of the cell after delithiation (Figure 4c), indicating that the active material has good affinity (low interface energy) with the surface of the carbon wall. Also, this morphology maximizes its interface area with carbon. This can also be observed in large-area TEM images (Figure 4d and 4e). The good affinity and large interface area of the active material can explain the low polarization of the hybrid cellular nanosheets observed in cyclic voltammetry in Figure 3d. TEM images in Figure 4f and 4g were taken from the same location of the nanosheets before and after the lithiation and delithiation cycle. Comparing those two images, it is clearly seen that the carbon cellular structure is hardly affected by the large volume change of SnO_2-based active material inside of the cells. The spatial distribution of SnO_2-based active material after 20 cycles was measured by energy-dispersive X-ray spectroscopy (EDX) mapping of Sn and dark-field TEM (Figures 4h–j, see Figure S12 for large-area STEM image). Both elemental mapping and dark-field images confirm that SnO_2-derived active material is well confined in the cells without aggregation or leakage from the cells.

The TEM data discussed above reveal that the excellent electrochemical performance of SnO_2–carbon cellular nano-

DOI: 10.1021/jacs.5b03673
J. Am. Chem. Soc. 2015, 137, 11954–11961

sheets is attributed to their unique hybrid structure (Figure 5). Because each cell has enough room for the volume change of SnO_2 NPs, the carbon wall does not exert mechanical stress to the SnO_2-based active material confined in the cell even when the active material is fully lithiated to the maximum volume expansion. The cubic shape of the cells allows the higher packing density as well as the larger interface area of the loaded active material with carbon, compared to the spherical shape with the same volume (see Figure S14 and the corresponding text in Supporting Information). The well-ordered cellular structure of the nanosheets is rigid enough to confine the active material inside of the cell during cycling, keeping the mechanical integrity of the electrode film. The Li-ion diffusion length can be as short as 100 nm in the thickness direction of the nanosheets. At the same time, facile electron transport is possible through the carbon network of the nanosheets. Consequently, the structure of the hybrid cellular nanosheets is well optimized for the high-performance anodes in terms of the specific capacity, cycling stability, and rate capability.

CONCLUSION

We developed a practical synthetic method to prepare SnO_2–carbon hybrid cellular nanosheets that exhibit outstanding electrochemical performance for nearly all key aspects of lithium-ion battery electrodes. Carbon cellular nanosheets have unique cubic cavity cells forming a well-ordered close-packed array, and numerous electrochemically active materials can be controllably immobilized in the carbon cells using various methods including the "ship-in-a-bottle" method. Cellular nanosheets loaded with SnO_2 NPs showed outstanding electrochemical performance as lithium-ion battery anodes. The specific capacity of SnO_2–carbon hybrid nanosheets was 913.9 mAh g^{-1} on average with a retention of 97.0% during 300 cycles. Also, when the cycling current density was increased from 200 to 3000 mA g^{-1}, the reversible capacity was decreased by only 20% from 941.3 to 745.5 mAh g^{-1}. This excellent performance can be compared with that of other similar structured hybrid nanostructures. For example, our previously reported ferrite–carbon hybrid nanosheets, which were used to prepare the carbon hybrid cellular nanosheets, exhibit a specific capacity of 600 mAh g^{-1} and 73% retention of initial capacity after 50 cycles.[52]

According to cyclic voltammetry, in situ XANES, and TEM analyses, such high performance is closely related to the cellular structure of the hybrid nanosheets. The cubic cells provide enough room to accommodate the large volume change of the active material as well as the large interface area between the loaded active material and the carbon wall. As a result, the hybrid structure shows high reversibility of lithiation and delithiation. In addition, well-ordered rigid cellular nanosheet structure ensures the mechanical integrity and facile Li-ion and electron transport.

In conclusion, we show that very effective hybrid nanostructured electrode material can be prepared via a relatively simple procedure. Because many different kinds of materials can be immobilized in the carbon cellular nanosheets, the resulting hybrid cellular nanosheets can be applied to various areas including electrochemical devices and catalysis.

EXPERIMENTAL SECTION

Materials. $MnCl_2{\cdot}4H_2O$, $FeCl_3{\cdot}6H_2O$, Na_2SO_4, and $SnCl_2$ were purchased from Sigma-Aldrich. Sodium oleate and tetraphenyltin were purchased from TCI and Alfa-Aesar, respectively. All reagents were used without further purification.

Preparation of Carbon Cellular Nanosheets. Iron–oleate and manganese–oleate precursors were synthesized following a previously reported method.[51,52] For the synthesis of carbon cellular nanosheets, 18.0 g (20 mmol) of iron–oleate and 6.2 g (10 mmol) of manganese–oleate were mixed with 150 g of Na_2SO_4 and the mixture was heated at 500 °C under argon flow (100 sccm) for 5 h. After heating, carbon nanosheets embedded with manganese ferrite nanocubes were washed with hot water for 2 h to remove Na_2SO_4, and the manganese ferrite nanocubes were etched with hydrochloric acid. Carbon cellular nanosheets were collected from the aqueous suspension by centrifugation and thermally treated at 800 °C for 5 h to improve the conductivity of carbon.

Synthesis of SnO_2–Carbon Cellular Nanosheets and SnO_2 Nanosheets. In the vapor deposition method, 100 mg of carbon cellular nanosheets and 800 mg of tetraphenyltin were mixed with a mortar and pestle. The mixture was heated at 350 °C for 3 h under vacuum. As-synthesized SnO_2–carbon nanosheets were used without additional purification. SnO_2 nanosheets were prepared by annealing SnO_2–carbon hybrid cellular nanosheets at 500 °C for 5 h under air.

Characterization. TEM analysis was performed using a JEOL JEM-2100F (Jeol). STEM and EDS mapping images were obtained with a Tecnai F20 (FEI) equipped with an EDAX Tecnai 136-5 detector. SEM analysis was carried out on a SUPRA 55VP FE-SEM (Carl Zeiss). XPS measurement was done by a Sigma Probe instrument (ThermoFisher Scientific) with Al Kα (1486.8 eV) as the X-ray source. The pass energy is 100 eV for wide scan and 20 eV for narrow scan. XPS data analysis was performed using Avantage software. X-ray diffraction was measured by a D/Max-3C diffractometer (Rigaku) equipped with a rotating anode and a Cu Kα radiation source (λ = 0.15418 nm), nitrogen isotherm by a 3FLEX surface characterization analyzer (Micromeritics), Raman spectrum by a T64000 spectrometer (Horiba scientific) with an excitation wavelength of 514 nm, and TGA by a Q5000 IR thermogravimetric analyzer (TA Instruments). Small-angle X-ray scattering (SAXS) data was measured in the 4C beamline of Pohang Light Source (PLS-II, South Korea).

Electrochemical Characterization. Working electrodes were prepared by coating copper foil with a slurry made of active material, super P, and polyvinylidene fluoride (70:15:15 wt %) in *n*-methyl-2-pyrrolidinone solvent and drying in a vacuum oven. After cooling, the electrode film on the foil was compressed with a press roller to improve the packing of active material. A 2016-type coin cell was assembled in an argon-filled glovebox. The electrolyte was 1.0 M $LiPF_6$ dissolved in ethylene carbonate and diethyl carbonate with a 1:1 volume ratio. The coin cells were galvanostatically charged and discharged in the voltage range of 0.01–3.0 V (vs Li^+/Li) with a WBCS3000 cycler (WanA Tech). Cyclic voltammetry was measured using the same instrument. The coin cell tests were carried out at 25 °C. Electrochemical impedance spectroscopy measurements were obtained with an ac signal amplitude of 5 mV over the frequency range from 100 kHz to 10 mHz. In order to observe the TEM images before and after the electrochemical test, a 2032-type coin cell was assembled using a TEM grid loaded with SnO_2–carbon hybrid cellular nanosheets as the working electrode (Figure S13). The TEM grid was removed from the cell after the electrochemical test and washed with diethyl carbonate. After drying the TEM grid, TEM images after the electrochemical test were obtained.

In Situ XANES Measurement. X-ray absorption spectroscopy was measured at the 8C nanoprobe XAFS beamline (BL8C) of PLS-II in the 3.0 GeV storage ring with a ring current of 300 mA. The beam source was a tapered in-vacuum undulator, and a Si(111) double-crystal monochromator was used. A secondary source aperture was used to adjust the beam size to be 0.3 mm (v) × 1 mm (h) in front of the ionization chambers. A high voltage of 3000 V was applied to the ionization chambers which were filled with a mixture gas of N_2 and Ar to measure X-ray intensity. Modified 2032-type coin cells were used for in situ XANES experiments. The coin cell was positioned so that the incident angle of the X-ray beam with respect to the surface of the

DOI: 10.1021/jacs.5b03673
J. Am. Chem. Soc. 2015, 137, 11954–11961

electrode is 45°. A passivated implanted planar silicon (PIPS) detector was mounted at the sample stage at a 90° position with respect to the incident beam. Sn K edge signal was measured using metallic Sn foil as a reference, and each scan took about 23 min. Data processing and analysis were performed using ATHENA of the IFEFFIT XAS data analysis suite.

■ ASSOCIATED CONTENT

Supporting Information

The Supporting Information is available free of charge on the ACS Publications website at DOI: 10.1021/jacs.5b03673.

TEM and small-angle X-ray scattering data of the carbon cellular nanosheets, low-magnification TEM image of SnO_2−carbon hybrid cellular nanosheets, wide-scan XPS spectra and TGA plots of the nanosheets, TEM images and XRD data of SnO_2 nanosheets, initial charge−discharge voltage profile, standard XANES data of Sn metal, SnO, and SnO_2, impedance spectra, large-area STEM image after cycles (PDF)

■ AUTHOR INFORMATION

Corresponding Authors

*ysung@snu.ac.kr.

*thyeon@snu.ac.kr.

Author Contributions

⊥S.-H.Y. and D.J.L. contributed equally to this work.

Notes

The authors declare no competing financial interest.

■ ACKNOWLEDGMENTS

T.H. acknowledges the financial support by IBS-R006-D1. Y.-E.S. acknowledges the financial support by IBS-R006-G1.

■ REFERENCES

(1) Tarascon, J.-M.; Armand, M. *Nature* **2001**, *414*, 359−367.

(2) Bruce, P. G.; Freunberger, S. A.; Hardwick, L. J.; Tarascon, J.-M. *Nat. Mater.* **2012**, *11*, 19−29.

(3) Kang, K.; Meng, Y. S.; Breger, J.; Grey, C. P.; Ceder, G. *Science* **2006**, *311*, 977−980.

(4) Zhao, X.; Sánchez, B. M.; Dobson, P. J.; Grant, P. S. *Nanoscale* **2011**, *3*, 839−855.

(5) Ji, X.; Lee, K. T.; Nazar, L. F. *Nat. Mater.* **2009**, *8*, 500−506.

(6) Chen, Y.; Freunberger, S. A.; Peng, Z.; Fontaine, O.; Bruce, P. G. *Nat. Chem.* **2013**, *5*, 489−494.

(7) Bruce, P. G.; Scrosati, B.; Tarascon, J.-M. *Angew. Chem., Int. Ed.* **2008**, *47*, 2930−2946.

(8) Aricò, A. S.; Bruce, P.; Scrosati, B.; Tarascon, J.-M.; van Schalkwijk, W. *Nat. Mater.* **2005**, *4*, 366−377.

(9) Guo, Y.-G.; Hu, J.-S.; Wan, L.-J. *Adv. Mater.* **2008**, *20*, 2878−2887.

(10) Wu, H. B.; Chen, J. S.; Hng, H. H.; Lou, X. W. *Nanoscale* **2012**, *4*, 2526−2542.

(11) Ji, L.; Lin, Z.; Alcoutlabi, M.; Zhang, X. *Energy Environ. Sci.* **2011**, *4*, 2682−2699.

(12) Chan, C. K.; Peng, H.; Liu, G.; McIlwrath, K.; Zhang, X. F.; Huggins, R. A.; Cui, Y. *Nat. Nanotechnol.* **2008**, *3*, 31−35.

(13) Teki, R.; Datta, M. K.; Krishnan, R.; Parker, T. C.; Lu, T.-M.; Kumta, P. N.; Koratkar, N. *Small* **2009**, *5*, 2236−2242.

(14) Wu, H.; Chan, G.; Choi, J. W.; Ryu, I.; Yao, Y.; McDowell, M. T.; Lee, S. W.; Jackson, A.; Yang, Y.; Hu, L.; Cui, Y. *Nat. Nanotechnol.* **2012**, *7*, 310−315.

(15) Park, M.-H.; Kim, M. G.; Joo, J.; Kim, K.; Kim, J.; Ahn, S.; Cui, Y.; Cho, J. *Nano Lett.* **2009**, *9*, 3844−3847.

(16) Jung, S. C.; Choi, J. W.; Han, Y.-K. *Nano Lett.* **2012**, *12*, 5342−5347.

(17) Wang, X.-L.; Han, W.-Q.; Chen, H.; Bai, J.; Tyson, T. A.; Yu, X.-Q.; Wang, X.-J.; Yang, X.-Q. *J. Am. Chem. Soc.* **2011**, *133*, 20692−20695.

(18) Park, M.-H.; Cho, Y.; Kim, K.; Kim, J.; Liu, M.; Cho, J. *Angew. Chem., Int. Ed.* **2011**, *50*, 9647−9650.

(19) Chockla, A. M.; Klavetter, K. C.; Mullins, C. B.; Korgel, B. A. *ACS Appl. Mater. Interfaces* **2012**, *4*, 4658−4664.

(20) Kravchyk, K.; Protesescu, L.; Bodnarchuk, M. I.; Krumeich, F.; Yarema, M.; Walter, M.; Guntlin, C.; Kovalenko, M. V. *J. Am. Chem. Soc.* **2013**, *135*, 4199−4202.

(21) Park, M.-S.; Wang, G.-X.; Kang, Y.-M.; Wexler, D.; Dou, S.-X.; Liu, H.-K. *Angew. Chem., Int. Ed.* **2007**, *46*, 750−753.

(22) Lou, X. W.; Wang, Y.; Yuan, C.; Lee, J. Y.; Archer, L. A. *Adv. Mater.* **2006**, *18*, 2325−2329.

(23) Kim, C.; Noh, M.; Choi, M.; Cho, J.; Park, B. *Chem. Mater.* **2005**, *17*, 3297−3301.

(24) Huang, J. Y.; Zhong, L.; Wang, C. M.; Sullivan, J. P.; Xu, W.; Zhang, L. Q.; Mao, S. X.; Hudak, N. S.; Liu, X. H.; Subramanian, A.; Fan, H.; Qi, L.; Kushima, A.; Li, J. *Science* **2010**, *330*, 1515−1520.

(25) Chen, J.; Xu, L.; Li, W.; Gou, X. *Adv. Mater.* **2005**, *17*, 582−586.

(26) Reddy, M. V.; Yu, T.; Sow, C.-H.; Shen, Z. X.; Lim, C. T.; Subba Rao, G. V.; Chowdari, B. V. R. *Adv. Funct. Mater.* **2007**, *17*, 2792−2799.

(27) Wu, X.-L.; Guo, Y.-G.; Wan, L.-J.; Hu, C.-W. *J. Phys. Chem. C* **2008**, *112*, 16824−16829.

(28) Kim, H. S.; Piao, Y.; Kang, S. H.; Hyeon, T.; Sung, Y.-E. *Electrochem. Commun.* **2010**, *12*, 382−385.

(29) Vetter, J.; Novák, P.; Wagner, M. R.; Veit, C.; Möller, K.-C.; Besenhard, J. O.; Winter, M.; Wohlfahrt-Mehrens, M.; Vogler, C.; Hammouche, A. *J. Power Sources* **2005**, *147*, 269−281.

(30) Balakrishnan, P. G.; Ramesh, R.; Prem Kumar, T. *J. Power Sources* **2006**, *155*, 401−414.

(31) Arora, P.; White, R. E.; Doyle, M. *J. Electrochem. Soc.* **1998**, *145*, 3647−3667.

(32) Zheng, R.; Meng, X.; Tang, F.; Zhang, L.; Ren, J. *J. Phys. Chem. C* **2009**, *113*, 13065−13069.

(33) Liu, N.; Wu, H.; McDowell, M. T.; Yao, Y.; Wang, C.; Cui, Y. *Nano Lett.* **2012**, *12*, 3315−3321.

(34) Wang, Z.; Luan, D.; Madhavi, S.; Hu, Y.; Lou, X. W. *Energy Environ. Sci.* **2012**, *5*, 5252−5256.

(35) Lou, X. W.; Li, C. M.; Archer, L. A. *Adv. Mater.* **2009**, *21*, 2536−2539.

(36) Lou, X. W.; Deng, D.; Lee, J. Y.; Archer, L. A. *Chem. Mater.* **2008**, *20*, 6562−6566.

(37) Lin, Y.-S.; Duh, J.-G.; Hung, M.-H. *J. Phys. Chem. C* **2010**, *114*, 13136−13141.

(38) Park, Y.; Choi, N.-S.; Park, S.; Woo, S. H.; Sim, S.; Jang, B. Y.; Oh, S. M.; Park, S.; Cho, J.; Lee, K. T. *Adv. Energy Mater.* **2013**, *3*, 206−212.

(39) Lee, K. T.; Jung, Y. S.; Oh, S. M. *J. Am. Chem. Soc.* **2003**, *125*, 5652−5653.

(40) Zhang, W.-M.; Hu, J.-S.; Guo, Y.-G.; Zheng, S.-F.; Zhong, L.-S.; Song, W.-G.; Wan, L.-J. *Adv. Mater.* **2008**, *20*, 1160−1165.

(41) Yu, Y.; Gu, L.; Wang, C.; Dhanabalan, A.; van Aken, P. A.; Maier, J. *Angew. Chem., Int. Ed.* **2009**, *48*, 6485−6489.

(42) Liang, J.; Yu, X.-Y.; Zhou, H.; Wu, H. B.; Ding, S.; Lou, X. W. *Angew. Chem., Int. Ed.* **2014**, *53*, 12803−12807.

(43) Xin, S.; Guo, Y.-G.; Wan, L.-J. *Acc. Chem. Res.* **2012**, *45*, 1759−1769.

(44) Jiao, Y.; Han, D.; Liu, L.; Ji, L.; Guo, G.; Hu, J.; Yang, D.; Dong, A. *Angew. Chem., Int. Ed.* **2015**, *54*, 5727−5731.

(45) Liu, N.; Lu, Z.; Zhao, J.; McDowell, M. T.; Lee, H.-W.; Zhao, W.; Cui, Y. *Nat. Nanotechnol.* **2014**, *9*, 187−192.

(46) Magasinski, A.; Dixon, P.; Hertzberg, B.; Kvit, A.; Ayala, J.; Yushin, G. *Nat. Mater.* **2010**, *9*, 353−358.

(47) Lee, S. H.; Yu, S.-H.; Lee, J. E.; Jin, A.; Lee, D. J.; Lee, N.; Jo, H.; Shin, K.; Ahn, T.-Y.; Kim, Y.-W.; Choe, H.; Sung, Y.-E.; Hyeon, T. *Nano Lett.* **2013**, *13*, 4249−4256.

DOI: 10.1021/jacs.5b03673
J. Am. Chem. Soc. 2015, 137, 11954−11961

(48) Zhou, X.; Yin, Y.-X.; Wan, L.-J.; Guo, Y.-G. *Adv. Energy Mater.* **2012**, *2*, 1086−1090.
(49) Jiao, Y.; Han, D.; Ding, Y.; Zhang, X.; Guo, G.; Hu, J.; Yang, D.; Dong, A. *Nat. Commun.* **2015**, *6*, 6420.
(50) Yu, S.-H.; Conte, D. E.; Baek, S.; Lee, D.-C.; Park, S.-K.; Lee, K. J.; Piao, Y.; Sung, Y.-E.; Pinna, N. *Adv. Funct. Mater.* **2013**, *23*, 4293−4305.
(51) Park, J.; An, K.; Hwang, Y.; Park, J.-G.; Noh, H.-J.; Kim, J.-Y.; Park, J.-H.; Hwang, N.-M.; Hyeon, T. *Nat. Mater.* **2004**, *3*, 891−895.
(52) Jang, B.; Park, M.; Chae, O. B.; Park, S.; Kim, Y.; Oh, S. M.; Piao, Y.; Hyeon, T. *J. Am. Chem. Soc.* **2012**, *134*, 15010−15015.
(53) Serna, P.; Gates, B. C. *Acc. Chem. Res.* **2014**, *47*, 2612−2620.
(54) Lee, J.; Lee, D.; Oh, E.; Kim, J.; Kim, Y.-P.; Jin, S.; Kim, H.-S.; Hwang, Y.; Kwak, J. H.; Park, J.-G.; Shin, C.-H.; Kim, J.; Hyeon, T. *Angew. Chem., Int. Ed.* **2005**, *44*, 7427−7432.
(55) Kang, E.; Jung, Y. S.; Cavanagh, A. S.; Kim, G.-H.; George, S. M.; Dillon, A. C.; Kim, J. K.; Lee, J. *Adv. Funct. Mater.* **2011**, *21*, 2430−2438.
(56) Zhu, S.; Zhou, H.; Hibino, M.; Honma, I.; Ichihara, M. *Adv. Funct. Mater.* **2005**, *15*, 381−386.
(57) Han, F.-D.; Yao, B.; Bai, Y.-J. *J. Phys. Chem. C* **2011**, *115*, 8923−8927.
(58) Marichy, C.; Donato, N.; Willinger, M.-G.; Latino, M.; Karpinsky, D.; Yu, S.-H.; Neri, G.; Pinna, N. *Adv. Funct. Mater.* **2011**, *21*, 658−666.
(59) Wang, H.; Robinson, J. T.; Diankov, G.; Dai, H. *J. Am. Chem. Soc.* **2010**, *132*, 3270−3271.
(60) Wang, D.; Li, X.; Wang, J.; Yang, J.; Geng, D.; Li, R.; Cai, M.; Sham, T.-K.; Sun, X. *J. Phys. Chem. C* **2012**, *116*, 22149−22156.
(61) Paek, S.-M.; Yoo, E.; Honma, I. *Nano Lett.* **2009**, *9*, 72−75.
(62) Wen, Z.; Wang, Q.; Zhang, Q.; Li, J. *Adv. Funct. Mater.* **2007**, *17*, 2772−2778.
(63) Wu, P.; Du, N.; Zhang, H.; Yu, J.; Yang, D. *J. Phys. Chem. C* **2010**, *114*, 22535−22538.
(64) Zhu, J.; Lei, D.; Zhang, G.; Li, Q.; Lu, B.; Wang, T. *Nanoscale* **2013**, *5*, 5499−5505.
(65) Courtney, I. A.; Dahn, J. R. *J. Electrochem. Soc.* **1997**, *144*, 2045−2052.
(66) Han, F.; Li, W.-C.; Li, M.-R.; Lu, A.-H. *J. Mater. Chem.* **2012**, *22*, 9645−9651.
(67) Kim, H.; Park, G. O.; Kim, Y.; Muhammad, S.; Yoo, J.; Balasubramanian, M.; Cho, Y.-H.; Kim, M.-G.; Lee, B.; Kang, K.; Kim, H.; Kim, J. M.; Yoon, W.-S. *Chem. Mater.* **2014**, *26*, 6361−6370.

DOI: 10.1021/jacs.5b03673
J. Am. Chem. Soc. 2015, 137, 11954−11961